PAPER

NSTX-U theory, modeling and analysis results

To cite this article: W. Guttenfelder *et al* 2022 *Nucl. Fusion* **62** 042023

IOP Publishing | International Atomic Energy Agency Nuclear Fusion

Nucl. Fusion **62** (2022) 042023 (17pp) https://doi.org/10.1088/1741-4326/ac5448

NSTX-U theory, modeling and analysis results

W. Guttenfelder[1,*], D.J. Battaglia[1], E. Belova[1], N. Bertelli[1], M.D. Boyer[1], C.S. Chang[1], A. Diallo[1], V.N. Duarte[1], F. Ebrahimi[1], E.D. Emdee[1], N. Ferraro[1], E. Fredrickson[1], N.N. Gorelenkov[1], W. Heidbrink[2], Z. Ilhan[3], S.M. Kaye[1], E.-H. Kim[1], A. Kleiner[1], F. Laggner[1], M. Lampert[1], J.B. Lestz[2], C. Liu[1], D. Liu[2], T. Looby[4], N. Mandell[1], R. Maingi[1], J.R. Myra[5], S. Munaretto[1], M. Podestà[1], T. Rafiq[3], R. Raman[6], M. Reinke[7], Y. Ren[1], J. Ruiz Ruiz[8], F. Scotti[9], S. Shiraiwa[1], V. Soukhanovskii[9], P. Vail[3], Z.R. Wang[1], W. Wehner[3], A.E. White[10], R.B. White[1], B.J.Q. Woods[11], J. Yang[1], S.J. Zweben[1], S. Banerjee[12], R. Barchfeld[13], R.E. Bell[1], J.W. Berkery[14], A. Bhattacharjee[1], A. Bierwage[15], G.P. Canal[16], X. Chen[10], C. Clauser[3], N. Crocker[17], C. Domier[13], T. Evans[18], M. Francisquez[1], K. Gan[4], S. Gerhardt[1], R.J. Goldston[1], T. Gray[19], A. Hakim[1], G. Hammett[1], S. Jardin[1], R. Kaita[1], B. Koel[20], E. Kolemen[20], S.-H. Ku[1], S. Kubota[17], B.P. LeBlanc[1], F. Levinton[21], J.D. Lore[19], N. Luhmann[13], R. Lunsford[1], R. Maqueda[22], J.E. Menard[1], J.H. Nichols[4], M. Ono[1], J.-K. Park[1], F. Poli[1], T. Rhodes[17], J. Riquezes[14], D. Russell[5], S.A. Sabbagh[14], E. Schuster[3], D.R. Smith[23], D. Stotler[1], B. Stratton[1], K. Tritz[24], W. Wang[1] and B. Wirth[4]

[1] Princeton Plasma Physics Laboratory, Princeton University, Princeton, NJ 08543, United States of America
[2] University of California at Irvine, Irvine, CA, United States of America
[3] Lehigh University, Bethlehem, PA, United States of America
[4] University of Tennessee, Knoxville, TN, United States of America
[5] Lodestar Research Corporation, Boulder, CO, United States of America
[6] University of Washington, Seattle, WA, United States of America
[7] Commonwealth Fusion Systems, Cambridge MA, United States of America
[8] Oxford University, Oxford, United Kingdom of Great Britain and Northern Ireland
[9] Lawrence Livermore National Laboratory, Livermore, CA, United States of America
[10] Plasma Science and Fusion Center, Massachusetts Institute of Technology, Cambridge, MA, United States of America
[11] University of York, York, United Kingdom of Great Britain and Northern Ireland
[12] College of William and Mary, Williamsburg VA, United States of America
[13] University of California at Davis, Davis, CA, United States of America
[14] Columbia University, New York, NY, United States of America
[15] National Institutes for Quantum and Radiological Science and Technology, Aomori, Japan
[16] Institute of Physics, University of São Paulo, São Paulo, Brazil
[17] University of California at Los Angeles, Los Angeles, CA, United States of America
[18] General Atomics, San Diego, CA, United States of America
[19] Oak Ridge National Laboratory, Oak Ridge, TN, United States of America
[20] Princeton University, Princeton, NJ, United States of America
[21] Nova Photonics, Princeton, NJ, United States of America
[22] X Science LLC, Plainsboro, NJ, United States of America
[23] University of Wisconsin, Madison, WI, United States of America
[24] Johns Hopkins University, Baltimore, MD, United States of America

[*] Author to whom any correspondence should be addressed.

E-mail: wgutten@pppl.gov and gutten@pppl.gov

Received 1 June 2021, revised 17 August 2021
Accepted for publication 9 February 2022
Published 30 March 2022

Abstract

The mission of the low aspect ratio spherical tokamak NSTX-U is to advance the physics basis and technical solutions required for optimizing the configuration of next-step steady-state tokamak fusion devices. NSTX-U will ultimately operate at up to 2 MA of plasma current and 1 T toroidal field on axis for 5 s, and has available up to 15 MW of neutral beam injection power at different tangency radii and 6 MW of high harmonic fast wave heating. With these capabilities NSTX-U will develop the physics understanding and control tools to ramp-up and sustain high performance fully non-inductive plasmas with large bootstrap fraction and enhanced confinement enabled via the low aspect ratio, high beta configuration. With its unique capabilities, NSTX-U research also supports ITER and other critical fusion development needs. Super-Alfvénic ions in beam-heated NSTX-U plasmas access energetic particle (EP) parameter space that is relevant for both α-heated conventional and low aspect ratio burning plasmas. NSTX-U can also generate very large target heat fluxes to test conventional and innovative plasma exhaust and plasma facing component solutions. This paper summarizes recent analysis, theory and modelling progress to advance the tokamak physics basis in the areas of macrostability and 3D fields, EP stability and fast ion transport, thermal transport and pedestal structure, boundary and plasma material interaction, RF heating, scenario optimization and real-time control.

Keywords: NSTX-U, NSTX, overview

(Some figures may appear in colour only in the online journal)

1. Introduction

The mission of the spherical tokamak NSTX-U [1, 2] is to advance the physics basis and technical solutions required for optimizing the configuration of next-step steady-state tokamak fusion devices. The low aspect ratio ($A = R/a < 2$) spherical tokamak (ST) configuration provides a potentially transformative route to more compact and possibly lower cost fusion pilot plant concepts [3–6]. Results from many MW-class auxiliary-heated STs (START [7], NSTX [8], MAST [9], Globus-M [10]) have demonstrated access to stable operation at high beta as predicted by theory. They also observed normalized energy confinement times that increase with decreasing collisionality [11–15], which scales favorably when projecting to conditions required for steady-state (100% non-inductive) net-electric fusion pilot plants. Following these results, NSTX was upgraded to extend and validate the physics of low-A confinement and stability limits to lower collisionality needed to project to burning plasma regimes with increased confidence. NSTX-U will operate at up to 2 MA of plasma current and 1 T of toroidal field on axis for 5 s 15 MW of neutral beam injection (NBI) power is available at different tangency radii, along with 6 MW of high harmonic fast wave (HHFW) power. With these new capabilities, NSTX-U aims to demonstrate high bootstrap fraction ($f_{\rm BS} > 0.7$), 100% non-inductive regimes to explore the low-A ($A = 1.7$), high beta ($\beta_{\rm N} > 5$), highly shaped ($\kappa \leqslant 2.7$, $\delta \leqslant 0.8$) approach to steady-state operation.

Enabled by its unique capabilities, NSTX-U research also supports ITER and other critical fusion development needs. Neutral beam fast-ion phase space overlaps the alpha-particle regimes expected at low and high aspect ratio (including ITER), due to fast ions accessing super-Alfvénic velocities (at relatively low field) over a wide-range of achievable fast ion beta. Coupled with high heating power, the strongly-shaped, low-A configuration also leads to very high plasma facing component (PFC) target fluxes (>30 MW m^{-2}) allowing evaluation of integrated tests of advanced PFC solutions, such as liquid lithium divertors. More generally, unifying the validated understanding of core and boundary physics developed at low-A with that at conventional-A will enable more robust configuration optimization of future concepts.

During the period of the NSTX-U Recovery Project, now in the construction and installation phase [16] following initial operations in 2016 [17, 18], there has been considerable analysis, theory and modelling progress to develop new understanding and tools that will support future operation and experiments, and to advance the low aspect ratio tokamak physics basis for confidently predicting next-step devices. This paper summarizes the most recent results in these areas subsequent to the 2018 Fusion Energy Conference [19]. Validating the mechanisms responsible for core thermal transport, fast ion transport, and H-mode pedestal structure has advanced understanding of achievable confinement and performance limits at low-aspect ratio. Improved modeling of global MHD

and energetic particle (EP) instabilities, as well as developments in integrated predictive modeling and real-time control methods, provide tools to help optimize scenarios in future NSTX-U experiments. Observations and analysis of scrape-off-layer (SOL) and divertor turbulence have provided detailed measurements and new insights into dynamics that influence L/H transition, ELM onset, inter-ELM turbulence, and turbulence in the SOL-divertor region. New simulation and modeling capabilities have been developed to predict boundary turbulence and SOL width, which influences particle and heat loads to divertor targets, and to predict operational limits of PFCs.

2. Macrostability and 3D fields

Global kink and tearing modes often arose in high-β long-pulse NSTX plasmas, leading to enhanced fast-ion loss or redistribution, reduced core rotation, H $\rightarrow$ L back-transitions, and possibly disruptions [20]. To help identify stable operating regimes in NSTX-U, the resistive DCON (RDCON) code has been updated to calculate tearing mode stability (Δ') in full toroidal geometry and benchmarked against MARS and PEST3 simulations [21, 22]. Enabled by high numerical efficiency, RDCON is used to identify ranges in β_N and q_{95} that are stable to both $n = 1$ external kink and 2/1 tearing modes. The Corsica equilibrium code [23] is used to vary the safety factor and pressure profiles. As an example, a model NSTX-U H-mode equilibrium at full field and high power (1.0 T, 2.0 MA, 12 MW NBI) is considered assuming a safety factor at the magnetic axis that is fixed just above unity. Figure 1 shows the $n = 1$ external kink can reach higher β_N at a few values of q_{95}, while Δ' at the $q = 2$ surface indicates the 2/1 tearing mode has a continuous (in β_N) window of stability at $q_{95} \sim 7$–8. Taken together, the simulations for this example predict an operating window around $q_{95} \sim 7.5$, with $\beta_N \sim 3$ or possibly higher, that can be simultaneously stable to both modes. Additional scans will be used to more broadly guide NSTX-U operations to optimize high performance plasmas including ramp-up. The more tangential NBI in NSTX-U provides additional flexibility to access $q_{min} > 2$ and optimize rotation profiles to further stabilize tearing modes.

Extensive metrology and plasma response modeling with IPEC [24] and M3D-C1 [25] have been conducted to quantify the strength and sensitivity of the various sources of error fields on NSTX-U [26]. The modeling has been used to help inform tolerances on coil alignments in the NSTX-U Recovery Project by considering the effect of misalignments on resonant fields and on perturbations to the magnetic pitch on PFCs. The alignment tolerances of the PF coils near the outer midplane are found to be set by a constraint on the amplitude of the 2/1 resonant error field, while the tolerances of the PF coils near the divertor regions are found to be set by a constrain on the fractional perturbation of the magnetic field pitch at the divertor plates. Additional calculations show that misalignments in PF coils cause strike-point splitting and can extend divertor footprints. For expected error field amplitudes the strike point

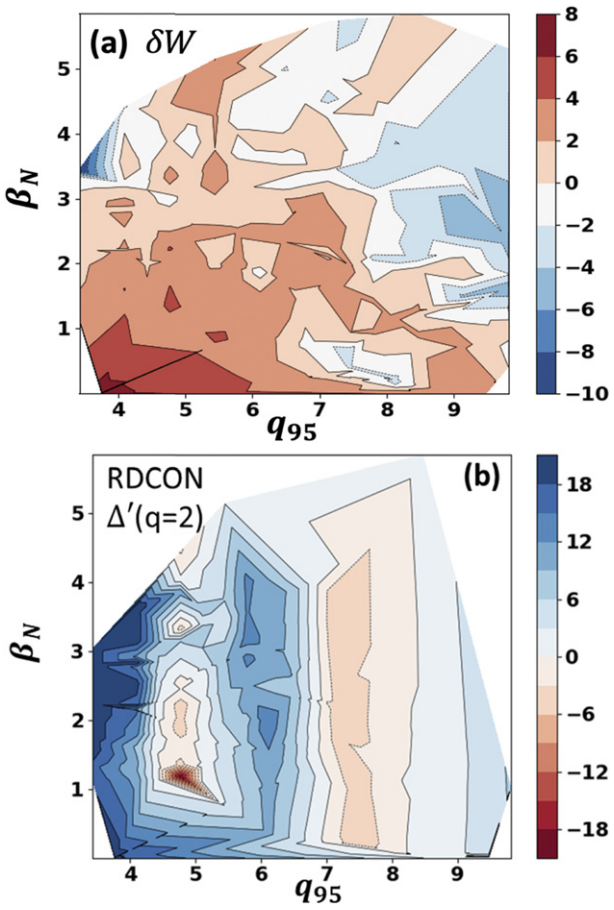

Figure 1. (*a*) $n = 1$ external kink stability ($\delta W > 0$, stable) and (*b*) 2/1 tearing stability ($\Delta' < 0$, stable), as a function of q_{95} and β_n for a 2 MA, 1 T, 12 MW NSTX-U scenario with q_{min} just above unity.

locations are contained within the divertor region designed to handle high heat fluxes [27].

Disruption mitigation simulations have been carried out for NSTX and NSTX-U equilibria using the M3D-C1 code to better understand how to optimize disruption mitigation in NSTX-U and other tokamaks. Using the recently incorporated KPRAD ionization/radiation model [28, 29] and a wall model with realistic resistivity [30], simulations explore how the presence of impurities in vertically unstable plasmas affect thermal and current quench timescales and the electromagnetic loads on the vacuum vessel. With a large quantity of impurities, a rapid reduction in stored thermal energy is predicted, as well as the onset of stochastic magnetic fields due to non-axisymmetric MHD instabilities. While the current quench also occurs more rapidly, so does vertical displacement, with the result that a significant fraction of the plasma current remains when the plasma contacts the wall. Corresponding forces on the vessel (from both halo and eddy currents) are found to be comparable in the cases with and without impurities. Future work will consider cases with even greater quantities of impurities, in order to quantify how short the current quench time must be in order to avoid having significant plasma current present when the plasma contacts the wall. An additional study explored the possibility of using an electromagnetic pellet injection (EPI) capability in NSTX-U. An EPI

system could offer a fast response time and high enough pellet speed to deposit payloads in the plasma core [31, 32]. To model this, M3D-C1 simulations were performed using a new pellet injection module [28] in which a single C-pellet was rapidly injected into an NSTX-U-like plasma using a carbon ablation model. Preliminary 2D simulations in NSTX-U suggest that the carbon content in a 1 mm radius carbon pellet ($\sim 3.2 \times 10^{20}$ atoms) should be sufficient to radiate the full thermal energy of the plasma if entirely ablated [33].

3. Energetic particle physics

The phase-space-resolved reduced EP transport *kick* model has been extended to include low-frequency, non-Alfvénic perturbations and validated against a variety of instabilities such as sawteeth, kink/fishbones and neoclassical tearing modes [34, 35]. Recent analysis has further extended the application of the kick model to investigate the impact of the coupled $n = 1$ kink + 2/1 tearing modes on fast ion transport [36]. The kink/tearing eigenmode structures, inferred from a synthetic diagnostic using forward modelling of soft x-ray measurements, are used to compute a kick probably matrix via ORBIT [37] simulations. The fast ion loss and corresponding neutron rates are self-consistently predicted using TRANSP [38] and NUBEAM [39] with this kick probability matrix. Figure 2(*b*) illustrates the relative difference in neutron rate between simulation and experiment as the kink/tearing mode amplitude increases (figure 2(*a*)). It is shown that the relative difference is $\sim$10% when the modes are excluded. The difference is reduced when the kink/tearing modes are included, but only when they are treated as being phase-locked (as observed in experiment), as opposed to assuming uncorrelated randomly-phased modes as typically assumed for Alfvénic instabilities. Inspection of the simulations indicates a transport channel forms between the phase space islands of kink and tearing modes through which fast ions are transported from near the magnetic axis to the $q = 2$ surface, and the sensitivity of this transport depends on the relative mode phase. Additional simulations scaling the mode amplitudes show that the experimentally inferred island width ($\sim$7 cm) appears to be sitting just below the onset of very large fast ion loss caused by orbit stochasticization (figure 2(*c*)). This suggests that the tearing mode island growth may be limited due to the interaction with kink mode and fast ions. A kinetic fast-ion module for M3D-C1 has been recently developed to simulate the self-consistent interaction between multiple MHD modes and fast ion dynamics [40].

Chirping and avalanches due to Alfvén eigenmodes (AEs) can degrade performance and lead to damaged PFCs from excessive fast ion redistribution and losses. Previous analysis has indicated that chirping is more prominent in NSTX than in conventional tokamaks as the high-beta, low-aspect ratio equilibrium sufficiently weakens ion-scale turbulence that can otherwise suppress highly coherent phenomena from taking place, such as the chirping behavior [41, 42]. Chirping, which is common in NSTX(-U) and cannot be ruled out for ITER [43], often serves as a gateway to avalanching scenarios that lead to massive fast ion ejection. Machine learning techniques have been used to automate and accelerate characterization of

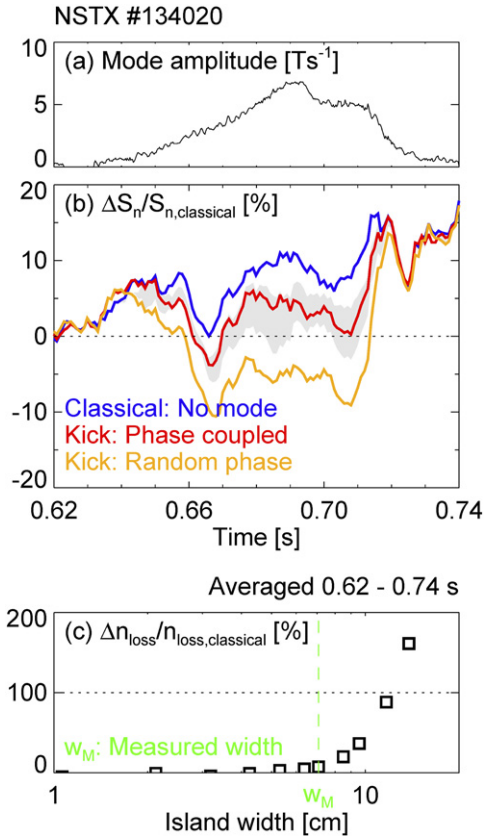

Figure 2. (*a*) Measured amplitude of coupled $n = 1$ kink + 2/1 tearing mode. (*b*) Relative difference in neutron rate between simulation and experiment, for classical losses only, or when including kick-model transport from the kink + tearing mode for both phase-coupled and random phase assumptions. (*c*) Predicted fast ion loss from phase-coupled kink + tearing mode for different tearing mode island widths. Reproduced from [36].

an extensive set of magnetic observations to further identify key correlations between the various observed characteristics (quiescent, fixed frequency, chirping, avalanching) and plasma parameters computed from TRANSP/NUBEAM (normalized NBI injection velocity, fast ion beta, safety factor profile) [44]. A correlation was found between higher $\beta_{beam}/\beta_{plasma}$ and the tendency for excitation of chirping and avalanches, in agreement with previous analysis [45]. However, the automated machine learning analysis found previously unidentified correlations, e.g. between plasma rotation and quiescence in TAE frequency bands, and between moments of the spectrograms and mode character.

Recent simulations and modeling have focused on understanding the nonlinear dynamics of chirping in NSTX(-U) using a guiding-center code (ORBIT) coupled with a delta-f formalism [46]. The simulations successfully reproduce observed chirping behavior (figure 3, top) with frequencies following the scaling predicted by adiabatic chirping theory, $\delta f = \pm(16\sqrt{2}/\pi^2 3\sqrt{3})\gamma_L\sqrt{\gamma_d t}$ [47]. The simulations confirm that, in addition to sufficient drive, an essential ingredient for chirping is the presence of strong mode damping that can be triggered e.g. by small equilibrium changes that cause the mode to contact the continuum. The chirping produces high

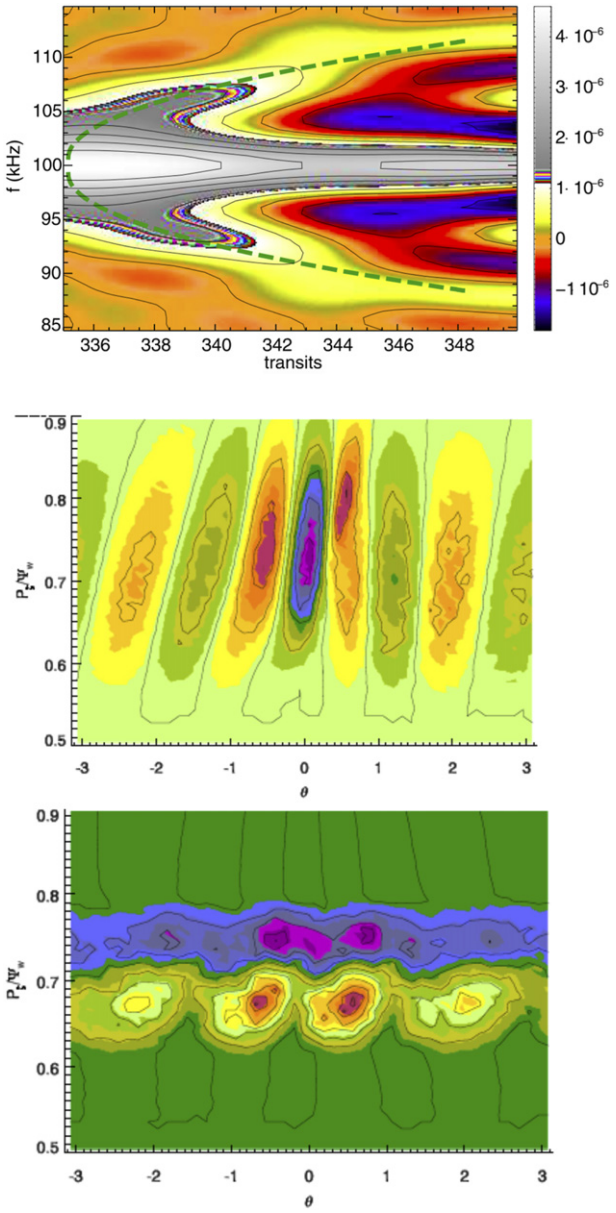

Figure 3. (Top) Evolution of chirping Alfven eigenmode frequency from ORBIT + delta-f simulations as a function of toroidal transit time of the energetic ion population. Dashed line indicates theoretical scaling of adiabatic chirping. Reprinted from [46], with the permission of AIP Publishing. (Middle, bottom) Contour plots of simulated δf vs poloidal coordinate (θ) and canonical angular momentum normalized to poloidal flux at the separatrix (P_ζ/ψ_W). The original resonance is located at around 0.7 of the normalized canonical toroidal momentum. At early times (middle), the distribution is modulated by the periodicity of the resonance chain of islands. At later times (bottom), holes and clumps form and detach from the resonance and propagate away from it. Reprinted from [48], with the permission of AIP Publishing.

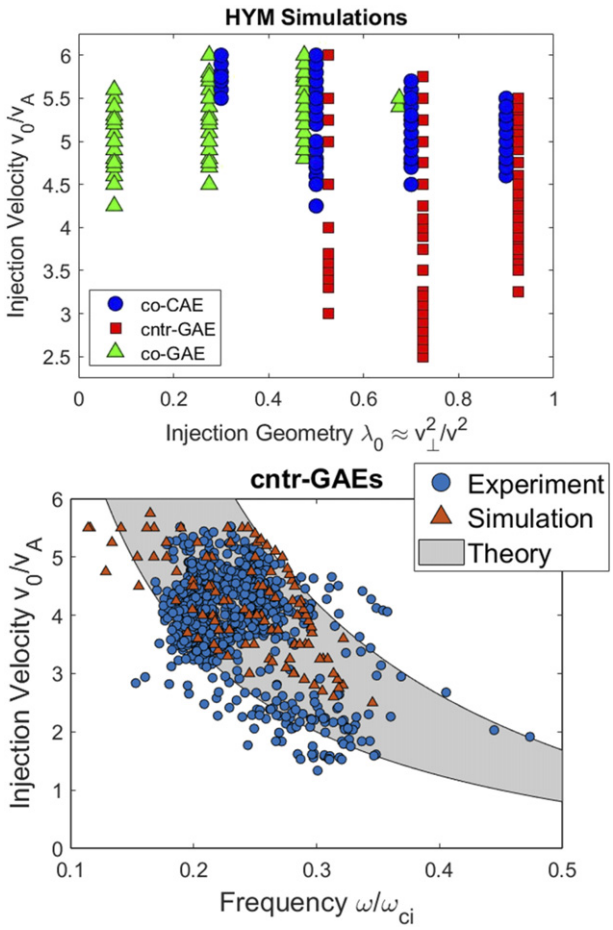

Figure 4. (Top) Unstable $|n| = 3$–12 GAE/CAE modes predicted by HYM as a function of the beam injection geometry $\lambda_0 \approx (v_\perp/v)^2$ and normalized velocity v_0/v_A. (Bottom) Comparison of experimentally observed counter-GAEs, unstable simulations, and theoretically predicted regimes, as a function of normalized injection velocity and frequency (ω/ω_{ci}). Reproduced courtesy of IAEA. Figure from [56]. Copyright (2021) IAEA.

density clumps, which propagate down the fast ion density gradient and low density holes that propagate up the density gradient away from the resonance (figure 3, middle and bottom panels). This flow of particles across the resonance provides an energy source and local gradients for sustained, repeated chirping [48, 49]. Detailed spectroscopic analyses [50] clarified the role of violent amplitude pulsations and phase jumps of the simulated chirping Alfvén mode. These phenomena are attributed to the beating of multiple non-normal modes associated with the presence of holes and clumps, and consequent half-period shift of mode phase. The radial propagation of these structures, responsible for sustained chirping, are in turn affected by the beats through feedback loops. Simulations were also used to investigate the onset of more deleterious avalanches observed in NSTX with super-Alfvénic beam ions ($V_{beam}/V_A > 1$), similar to fusion-generated α-particles ($V_\alpha/V_A > 1$) in burning plasmas like ITER. Avalanche onset is predicted to require the resonance overlap of multiple Alfvénic modes with sufficient amplitude. The simulations reproduce explosive growth of multiple modes for small changes in fast ion drive, indicating threshold-like behavior and the eventual inadequacy of the δf approach as wave-wave nonlinearities likely become important [51].

The presence of NBI-driven sub-cyclotron compressional (CAE) and global (GAE) AEs has previously been correlated with the core flattening of core thermal electron temperature in high power NSTX discharges [52]. The modes are hypothesized to influence electron thermal transport through

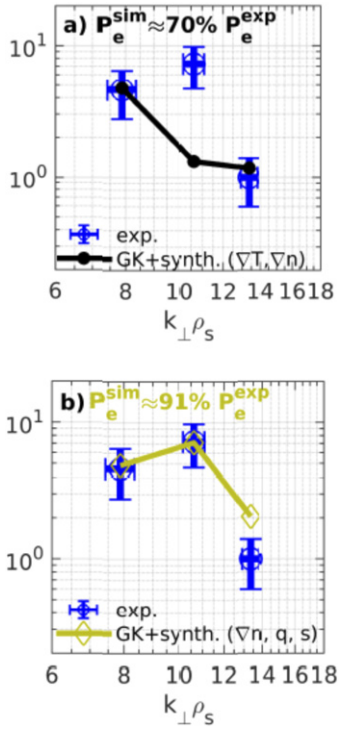

Figure 5. Power spectra from high-k microwave scattering measurements (symbols) and ETG simulations + synthetic diagnostic (lines) for two sets of input parameters, adjusted within experimental uncertainties. . Reproduced from [71]. © IOP Publishing Ltd. All rights reserved.

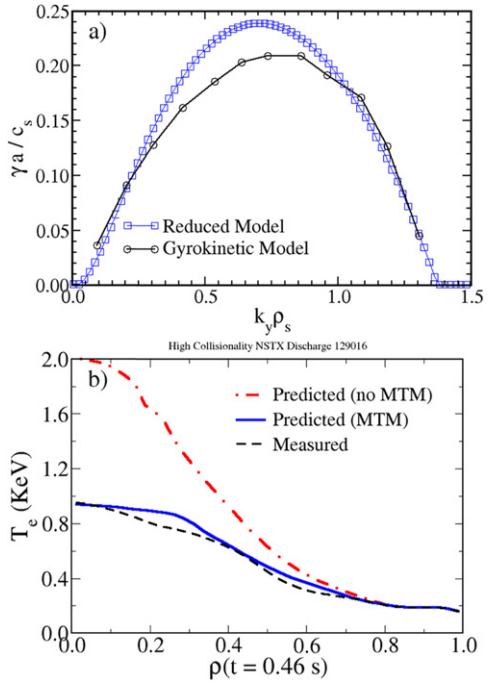

Figure 6. (*a*) Linear MTM growth rates from gyrokinetic simulations and reduced model. (*b*) Experimental T_e profiles compared to predictions without and with MTM transport model. Reprinted from [84], with the permission of AIP Publishing.

either diffusive-like transport due to electron orbit stochastization [53] or energy channeling from the core-localized GAE/CAE modes to a kinetic Alfven wave that is damped closer to the edge [54, 55]. Significant theoretical progress has been made in understanding the stability of these modes and identifying ways to stabilize them in order to test their impact on thermal confinement. Linear hybrid MHD/kinetic-fast-ion simulations (HYM) have been run for NSTX-like H-mode conditions [56] spanning a wide range of beam injection geometry, $\lambda_0 \approx (v_\perp/v)^2$, and velocity, v_0/v_A. Figure 4 (top) illustrates characteristic stability boundaries for three distinct types of modes: co- and counter-propagating GAEs, and co-propagating CAEs. In order to explain the simulated stability trends, a local analytic calculation of the fast ion drive was developed for an anisotropic beam distribution, including two-fluid dispersion and finite Larmor radius effects [57, 58]. With additional approximations, simple instability conditions are derived which constrain the beam injection geometry and velocity required to destabilize each type of mode. E.g., sub-cyclotron counter-propagating modes prefer more perpendicular beam injection, consistent with frequently observed counter-propagating GAEs in NSTX (beam injection geometries $\lambda_0 \sim 0.5$–0.7). Co-propagating modes are more easily destabilized by tangential injection due to the different signs of $\partial f_{beam}/\partial(v_\parallel/v)$ which drive their respective resonances. With the more tangential beams in NSTX-U ($\lambda_0 \sim 0.0$) it may therefore be possible to stimulate co-propagating GAEs (at low field $\sim$ large v_0/v_A) as a further validation of the theory. All types of modes have larger growth rates for larger values of v_0/v_A, but counter-GAEs can be excited at smaller values than either co-GAEs or co-CAEs (co-GAEs require a larger Doppler shift to satisfy the resonance condition; co-CAEs have a weaker fast ion drive overall), also consistent with their prevalence in NSTX(-U) observations. Excellent agreement is found between the theoretically predicted range of unstable frequencies, simulations, and a large experimental database of NSTX observations, as shown in figure 4 (bottom). Interestingly, the more tangential beams available in NSTX-U are predicted to have a stabilizing influence on counter-propagating GAEs, as already observed [59, 60] and reproduced in simulations [61]. This flexibility in beam injection geometry provides a mechanism by which to stabilize the modes and investigate their potential impact on core thermal transport. Recent simulations and experiments for conventional aspect ratio tokamaks suggest GAEs are present, and are also predicted to be unstable in ITER, although with much smaller growth rates and amplitudes than observed on NSTX [62].

A large number of detailed ion cyclotron emission (ICE) observations in NSTX and NSTX-U plasmas have recently been summarized [63, 64]. The measurements in NSTX(-U) using Mirnov coils identify many harmonics (1st–7th), with frequencies that scale with field but not density, ruling out Alfvénic modes. A number of distinct variations are observed, e.g. short bursts ($\leqslant$100 μs); longer, weaker bursts; or quasi-stationary states. The ICE frequency maps neither to the plasma edge, nor the magnetic axis as found on other tokamaks, and often appears correlated with a strong gradient in the density near the half-radius. No correlation between

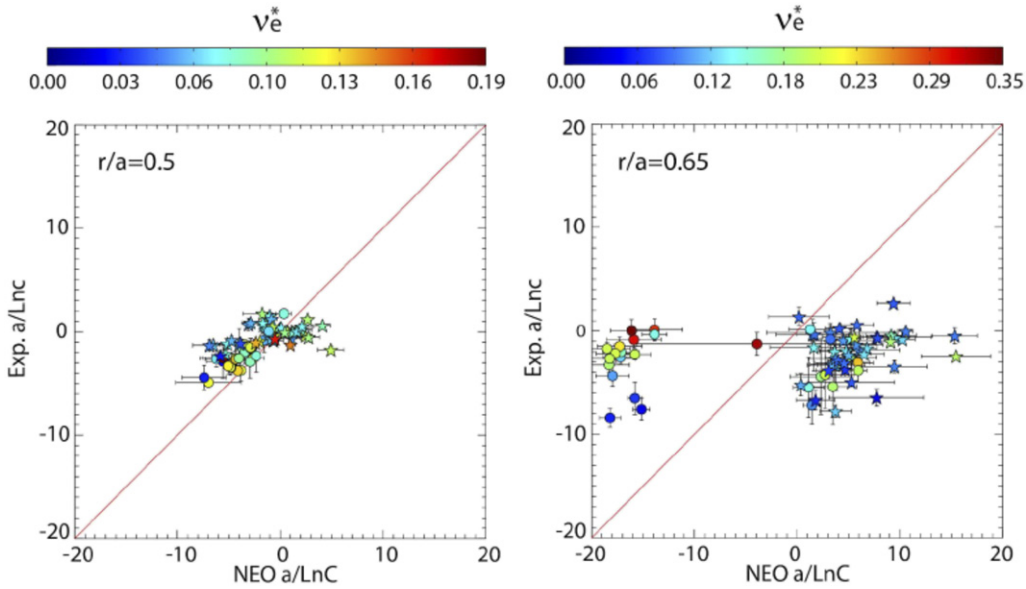

Figure 7. Comparison of experimentally measured normalized carbon density gradient vs neoclassical predictions at two different radii, $r/a = 0.5$ (left) and $r/a = 0.65$ (right). Symbol color correspond to normalized electron collisionality. Different symbols denote discharges that utilize different between-shot wall conditioning methods: boronization (circles), lithium (stars).

measured neutron rate and ICE amplitude is observed. While these observations challenge current theories, if understood, ICE could be considered for use as an additional α-particle relevant diagnostic for ITER and other burning plasmas.

4. Transport and pedestal structure

Previous high-k scattering measurements and gyrokinetic simulations suggest electron-scale electron temperature gradient (ETG) turbulence is present in many NSTX discharges and may therefore contribute to anomalous electron thermal losses in the core [65, 66]. The observed fluctuation amplitudes qualitatively scale with many theoretical expectations, however the transport predicted by nonlinear gyrokinetic simulations does not always reproduce experiment, almost always underpredicting transport [67]. To comprehensively validate ETG predictions, a novel synthetic diagnostic for high-k scattering has recently been developed to mimic the response function of the high-k scattering diagnostic [68]. Along with inferred energy fluxes, the measurements are used to constrain nonlinear GYRO [69] simulations in the outer region ($r/a = 0.7$) of a low power ($P_{\mathrm{NBI}} = 2$ MW) NSTX H-mode where electromagnetic modes are not predicted to play a significant role [70, 71]. Numerous nonlinear parameter scans were used to quantify the sensitivity of the predicted transport and high-k fluctuation spectra. Figure 5 provides two examples of predicted synthetic high-k spectra (lines) compared to experiment (symbols) at a radius of $r/a \approx 0.7$. By varying input parameters within uncertainties, agreement is found in predicted transport, the high-k spectra shape (figure 5(b)), as well as the relative change in amplitude for two different discharge times where the local density gradient is changed, giving confidence that ETG can in fact fully account for the observed transport and fluctuations in this case. These validated simulations can be used to qualify reduced ETG transport models. Additional local, ion scale simulations (GYRO) for this case illustrate the profile gradients sit just below the onset of very large, stiff ITG/TEM transport [72]. It is in these conditions (strong electron-scale drive, near-marginal ion-scales) that multi-scale effects have been found to be important in other tokamaks [73–75]. However, recent global ion-scale simulations (GTS) for this NSTX discharge predict that profile-shearing effects at the relatively large values of $\rho_* = \rho_s/a$ result in negligible ion-scale transport [76], consistent with the observation of neoclassical ion thermal transport, further supporting the dominance of electron-scale turbulence as the sole anomalous loss mechanism. A novel pseudo-local soft x-ray tomography diagnostic concept has been recently proposed to measure electron-scale temperature fluctuations (δT_e) [77]. Modeling based on simulations for an NSTX-U L-mode validation study [78] indicates the method could potentially be sensitive to the ETG fluctuation amplitudes predicted above and could therefore be used to provide additional constraint on validating ETG simulations.

In higher-power (typically $P_{\mathrm{NBI}} = 4$–6 MW), higher-β NSTX discharges, gyrokinetic simulations predict that electromagnetic instabilities like microtearing modes (MTM) and kinetic ballooning modes (KBM) are commonly unstable [12, 79–82], motivating the development of reduced transport models for these mechanisms. One recently developed reduced model for MTM transport [83] has been tested against a variety of high-β NSTX H-mode discharges [84]. The model makes improvements to older slab theory by treating arbitrary electron collisionality and including magnetic curvature effects. As a result, the model has been found to reproduce many of the linear gyrokinetic results predicted in NSTX discharges such as the variation of real frequency and growth rates with poloidal wavenumber (figure 6(a)), β, collisionality, and electron temperature and density gradients. The model

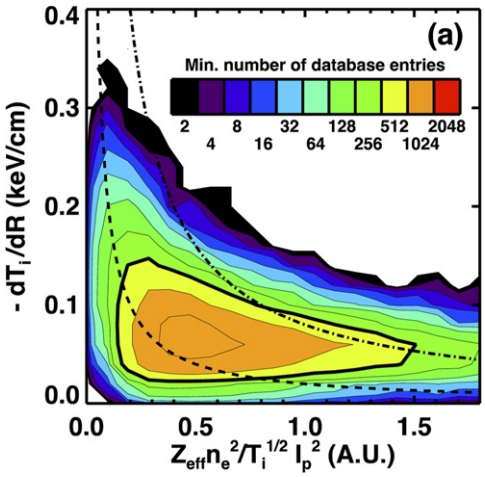

Figure 8. (Top). Database of maximum edge ∇T_i versus leading order terms of neoclassical transport. Dashed lines represent fixed $q_\mathrm{i,neo}$. Symbols are described in the text. Reprinted from [94], with the permission of AIP Publishing.

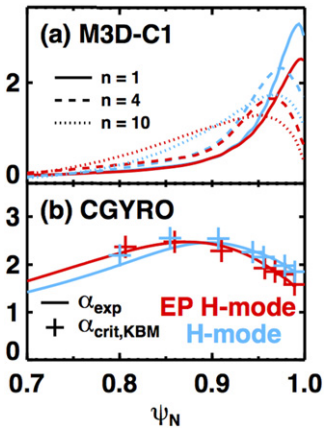

Figure 9. (*a*) MHD kink/peeling eigenfunctions (M3D-C1), and (*b*) normalized pressure gradient, α, from experiment (lines) and KBM thresholds (CGYRO, symbols) for both H and EPH mode. Reprinted from [94], with the permission of AIP Publishing.

also solves a nonlinear dispersion relation to self-consistently determine a saturated magnetic fluctuation amplitude, $\delta B/B_0$, which also agrees with some of the nonlinear simulation predictions. Using this saturated amplitude to compute stochastic transport following Rechester–Rosenbluth [85] provides the basis for the electron thermal transport model. The predicted T_e profiles using this model (in conjunction with the multi-mode model [86] within TRANSP) provides significantly improved agreement for a high collisionality NSTX H-mode discharge in (figure 6(*b*)) as compared to predictions without the MTM model. However, the model overpredicts transport at low collisionality, in part because the saturation model scales too weakly with collisionality (compared to nonlinear gyrokinetic simulations). The inability to reproduce the key scaling with collisionality motivates continued development of reduced transport models at high β and low aspect ratio that enable more accurate predictions for high-performance scenarios.

Previous observations have found that impurity transport of intrinsic carbon from the graphite PFCs is often near neoclassical predictions especially in high-collisionality H-modes where ion thermal transport is also neoclassical, whereas deviations from neoclassical were noted at low collisionality [87]. This analysis has been recently extended as part of a multi-machine impurity transport validation study [88], considering a much larger database of discharges used in confinement studies [12]. The analysis includes both ELMy and ELM-free discharges, the latter of which typically arise when using sufficient between-shot lithium wall conditioning that lowers recycling and changes pedestal profiles and corresponding stability. Carbon peaking (given by the local normalized gradients, $a/L_{n,\mathrm{C}}$) at mid-radius is found to be robustly consistent with neoclassical predictions using NEO including sonic rotation [89, 90]. However, significant deviations are observed farther out ($r/a \geqslant 0.65$) (figure 7). These deviations occur over a range of collisionality and do not appear to be strongly correlated with other physics parameters. However, there are distinct differences found for cases using boronization for wall conditioning (circles, typically ELMy) as opposed to evaporative lithium coatings (stars, typically ELM-free). We note that the analysis averages over ELMs (except large, irregular occurrences) as they are too frequent (>100 Hz) to resolve with profile measurements. For all times analyzed the global radiation is less than 20% of the injected power, although this can increase significantly later in the ELM-free discharges as carbon and higher-Z impurities gradually accumulate. Linear gyrokinetic analysis (CGYRO [91]) indicates that MTMs are unstable for high $\nu*$ (as is typical for high-β NSTX H-modes), however they produce negligible impurity transport ($\Gamma_\mathrm{c} \sim 0$). At lower $\nu*$, ballooning modes are found that predict carbon fluxes comparable in magnitude to the neoclassical predictions, but in the same direction and are therefore also unable to explain the discrepancy. Further analysis is required to understand what mechanisms explain the carbon profiles in these regions to develop robust quantitative predictions and methods to minimize accumulation.

The enhanced pedestal (EP) H-mode regime [92, 93] is an attractive ELM-free scenario for next-step Advanced Tokamak devices as it achieves $H_{98\mathrm{y},2} > 1.3$ at large Greenwald density fraction ($f_\mathrm{GW} > 0.7$), large bootstrap current fraction ($f_\mathrm{BS} > 0.7$) and large plasma current compared to the toroidal field ($I_\mathrm{p}/B_\mathrm{T} = 2$ MA/T). EP H-mode occurs on NSTX when the edge ion collisionality becomes sufficiently small ($\nu_{\mathrm{i}*} < 0.3$) such that a modest reduction in the edge density leads to a large reduction in the dominant neoclassical ion energy transport in the pedestal [94]. This is demonstrated in figure 8, where EP H-mode operating points (red and orange squares) are compared to a wide-pedestal H-mode discharge (blue points) and contours derived from a large database of NSTX discharges. The y-axis is the maximum edge ion temperature gradient (∇T_i) and the x-axis represents the leading terms of neoclassical scaling measured at the location of the maximum ∇T_i. The dashed lines indicate the neoclassical scaling for constant local ion heat flux (q_i). The filled contours indicate the regime most often accessed where 83% of the database entries reside within the thick black contour. EP H-mode is a regime that achieved

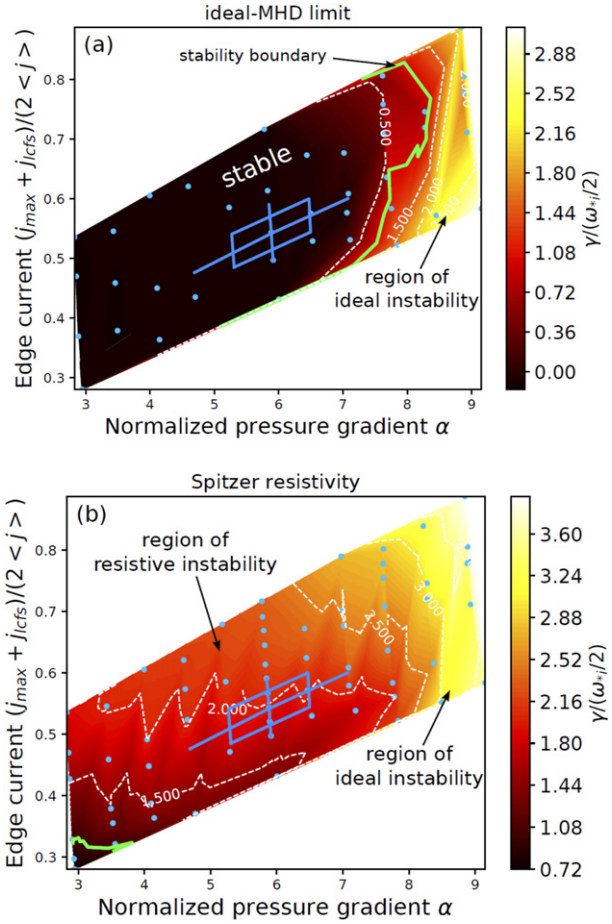

Figure 10. Normalized peeling-ballooning mode growth rates vs normalized pedestal pressure gradient, α, and current density j, for (a) ideal, and (b) resistive MHD simulations (M3D-C1). Experimental values shown by cross-hairs. The $\gamma/(\omega_{*i}/2) = 1$ stability boundary is shown by the green lines. Reproduced courtesy of IAEA. Figure from [101]. Copyright (2021) IAEA.

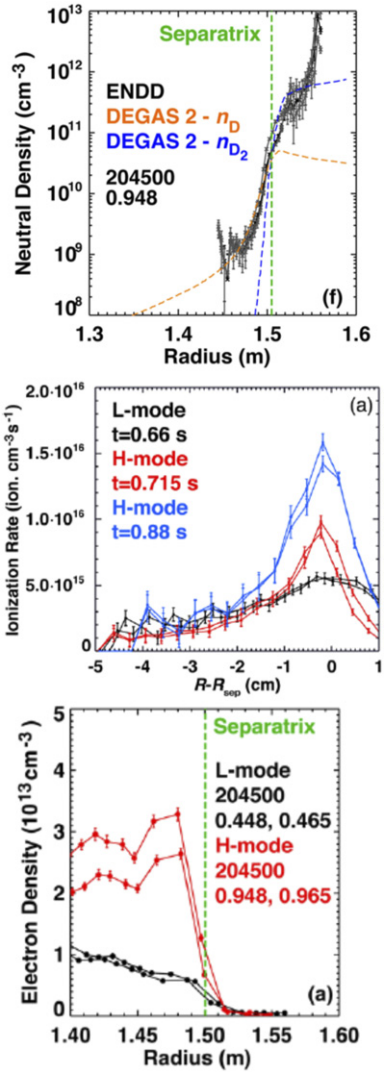

Figure 11. (Top) Measured atomic deuterium density compared to atomic and molecular deuterium density from DEGAS 2 modeling for an NSTX L-mode. (middle) Inferred ionization rates (upper-estimate) and (bottom) electron density profile in the edge of L- and H-mode phases of NSTX-U discharge. Reproduced courtesy of IAEA. Figure from [102]. Copyright (2021) IAEA.

the largest edge ∇T_i at uniquely low edge collisionality that was facilitated by low edge density, often accessed transiently following a large ELM. Linear MHD (M3D-C1) and gyrokinetic (CGYRO) simulations demonstrate that the pedestal profiles are unstable to kink/peeling modes (figure 9(a)) and sitting within 10% of KBM pressure gradient thresholds, $\alpha \sim \nabla p$ (figure 9(b)), respectively. Measurements with beam emission spectroscopy show that in the EP H mode, fluctuations shift to higher frequency and become more directed in the ion-diamagnetic direction, consistent with MHD-like instabilities. The presence of these pressure and current-driven instabilities provides a mechanism for enhanced particle transport that can lock-in the new profiles at increased ∇T_i and lower the edge density, with improved energy confinement. Gyrokinetic analysis also predicts a number of other modes are unstable (MTM, ETG, TEM) that likely contribute to establishing the pedestal profiles as they evolve to the KBM and kink/peeling instability thresholds.

The EPED model [95, 96], based on ideal MHD constraints, has had great success in predicting fully-developed ELMy H-mode pedestal structure at conventional aspect ratio. However, previous MHD stability calculations for fully-developed NSTX ELMy H-modes predict pedestals are stable or weakly unstable to ideal peeling-ballooning (P-B) modes, with growth rates normalized to half the ion-diamagnetic frequency $\gamma/(\omega_{*i}/2) \leqslant 0.1$ [92, 97–100], about ten times smaller than that predicted at conventional aspect ratio. Recent MHD simulations (M3D-C1) have been run to quantify the impact of various non-ideal effects [101]. An example is shown in figure 10 for a highly-shaped ELMy H-mode, where normalized growth rates (maximized over toroidal mode numbers $n = 1$–20) are computed for a range of self-consistent global equilibria that vary normalized pedestal pressure gradient and current density. Figure 10(a) illustrates that the experiment sits firmly in the range of stable ideal P-B modes. However, the modes become much more unstable when including Spitzer resistivity, and the unstable boundary moves to much lower

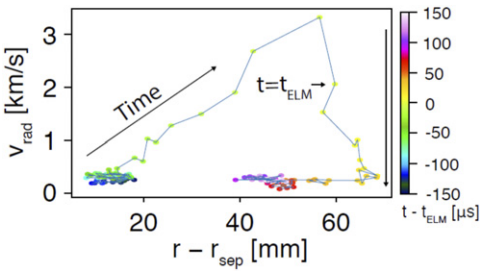

Figure 12. ELM filament radial velocity vs distance from separatrix. The time-to-ELM crash is given by the colorbar. Reprinted from [108], with the permission of AIP Publishing.

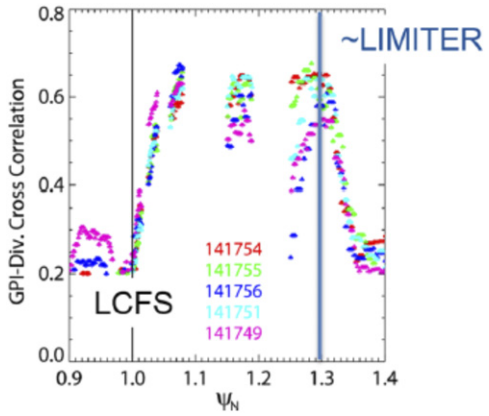

Figure 13. Maximum cross-correlation between upstream (GPI) and divertor target (Li I emission) fluctuations, plotted vs ψ_N. Reproduced courtesy of IAEA. Figure from [111]. Copyright (2020) IAEA.

edge current and pressure gradient (figure 10(*b*)). In the resistive limit, normalized growth rates for the experiment correspond to $\gamma/(\omega_{*i}/2) \sim 2$ indicating the resistive P-B modes are expected to be unstable, consistent with the ELMy H-mode regime. Similar simulations in DIII-D show resistivity has a much weaker effect. While resistivity is marginally smaller in the DIII-D case, the impact of aspect ratio, or more generally shaping, appears to play a non-negligible role in enhancing the role of resistivity for the NSTX discharges. Work towards a generalized pedestal structure model, including resistive MHD P-B stability and gyrokinetic KBM stability, is commencing and will be tested in NSTX-U to clarify the role of resistivity on establishing ELMy H-mode pedestal structure.

Deuterium atomic density n_D profiles were measured, and upper estimates of ionization rates inferred, on the LFS midplane of NSTX-U to enable fueling and pedestal transport studies [102]. Deuterium atomic densities are calculated by inverting the line-integrated D_α brightness measured by the 2D edge neutral density diagnostic (ENDD) camera. Ionization rates are obtained using atomic rate coefficients inferred using local n_e and T_e profiles, although they represent an upper estimate as the molecular contribution to D_α emissivity has been neglected. The assumptions used in the n_D and ionization rate derivations were validated using the Monte Carlo neutral transport code DEGAS 2 [103]. Good agreement in D_α emissivity profiles is found over a database of NSTX-U L- and H-modes, although far-SOL emission was under predicted possibly related to intermittent transport and uncertainties in molecular rates. The combined ENDD/DEGAS 2 analysis can generate n_D and n_{D2} radial profiles, extending the direct ENDD measurements in the core and SOL where emission is either too weak or dominated by molecular processes. Narrower n_D profiles are observed inside the separatrix in H-mode discharges. During the pedestal build up, an increase in peak ionization rate is observed with no significant change in either the pedestal or the ionization rate width (figure 11).

5. Boundary and PMI

Detailed SOL turbulence measurements using 2D gas puff imaging (GPI) [104] have been used to study dynamics associated with the L-H transition, ELM onset, inter-ELM turbulence, and divertor fluctuations. Understanding these phenomena is critical for understanding access to, and performance of, the H-mode pedestal, as well as the SOL heat flux width and corresponding divertor target peak heat fluxes that constrain plasma exhaust solutions and material choices in reactor conditions. Recent analysis and observations probe velocity dynamics prior to L-H transition [105], the appearance of 'wakes' following the filamentary dynamics observed in the inter-ELM period of H-mode plasmas [106], and correlations between global core MHD events and SOL filaments [107]. Two additional examples are highlighted here.

First, the characteristic behavior of SOL filaments observed before, during and after ELM crashes was analyzed exploiting the high temporal (2.5 μs) and spatial resolution (10 mm) of the GPI system [108]. A database of 159 ELM events (including type I, III and V ELMs) was generated from the 2010 NSTX measurement campaign. Data analysis methods were applied to estimate the number of filaments as well as their velocities, sizes, and distance from the separatrix. The distribution functions of each parameter were computed as a function of time relative to ELM onset ($t - t_{ELM}$), and the characteristic behavior of the ELM filament was determined from the evolution of the median of each distribution function. The analysis reveals that during the increased filamentary activity prior to the ELM crash, multiple filaments coalesce into a single, circular ELM filament structure that propagates outwards. Surprisingly, the radial velocity of the ELM filament increases $\sim$ linearly with distance from the separatrix in the $\sim$25 μs preceding the ELM crash (figure 12). This exponential acceleration ($V_{rad} = dr/dt \sim r$) of a single filament immediately prior to the ELM crash has never been observed. Following the ELM crash, which lasts for a median time of 100 μs, the radial velocities settle back to the pre-ELM level. The current-filament model [109], in which the filament is modelled as a current carrying wire, can explain coalescence of filaments, their circular shape, and the poloidal acceleration. It also predicts a repulsive force from the current hole forming in the plasma during the ELM crash that would cause radial acceleration. However, it cannot reproduce the exponential acceleration. A possible explanation could be that reconnecting edge

structures (plasmoids) emerge during the nonlinear dynamics of ELM filaments and contribute to current transport in the SOL [110].

Second, the correlation between divertor fluctuations and upstream turbulence (GPI) was studied in NSTX ohmic L-mode discharges [111]. The divertor target fluctuations were measured using a fast camera filtered for Li I emission, which localizes the observations to within a few mm of the divertor plate due to the short ionization mean free path. Divertor radial turbulence scale lengths as well as radial and poloidal turbulence propagation velocities are comparable to those on the low field side (LFS) midplane as measured by GPI. For each divertor radial location, the maximum cross correlation with every pixel in the GPI view was evaluated. The midplane/divertor correlation as a function of normalized poloidal flux for five discharges is shown in figure 13. Large correlations, up to 0.7, are observed in the far SOL. Approaching the separatrix ($\psi_N < 1.08$), divertor fluctuation levels and radial correlation lengths gradually decrease, as does the correlation between midplane and divertor turbulence. The reduction in correlation is consistent with that predicted in the electrostatic two-region blob model [112] due to X-point geometry and collisionality. A measured reduction in turbulence radial velocity is also expected from the two-region model, due to a reduction in the effective resistivity of the blob circuit, which could influence the SOL heat flux width and its scaling.

The various SOL turbulence observations provide some qualitative agreement with theory. However, the presence of strong amplitude intermittent filaments crossing from closed to open field lines, the possible role of electromagnetic effects (reconnection, drift-Alfvén dynamics), and the varying connection from upstream to divertor target drives the continued development of simulation capabilities.

Recent total-f gyrokinetic simulations using XGC [113] have reproduced empirical scalings of the SOL divertor heat-load width λ_q [114, 115] in NSTX, DIII-D, C-Mod, JET, and the 5 MA ITER H-mode plasmas, in the attached divertor condition [116–118]. However, significantly enhanced widths are projected for ITER 10 MA and 15 MA plasmas. Similar excursions are predicted for a projected NSTX-U full-current 2 MA discharge (figure 14), but not at lower current (1.5 MA). The larger heat-flux widths are predicted due to the onset of collisionless trapped electron mode (TEM) turbulence across the magnetic separatrix that exhibits streamer-like eddies as opposed to more blob-like turbulence (see insets in figure 14). The TEM turbulence is enhanced by reduced collisionality and either weakened $E \times B$ shearing rate at small ρ_{i*} (for ITER) or large trapped particle fraction (at low-A in NSTX-U). A supervised machine learning program has been used to find a unified formula from all simulation and experimental λ_q data that includes dependencies on ρ_{i*}, collisionality, and inverse aspect ratio: $\lambda_q^{ML} = \lambda_q^{Eich(14)}[1 + 1.08(10^{-2.5}\xi B_{pol,MP} a/\rho_{i,pol})^4]$, where $\xi = 1 + 2.3\,\Theta\,[(a/R_0)^{1/2}/\nu_{e*} - 1.75]$ and Θ is the heavy-side function. The NSTX-U simulations with enhanced λ_q predict a co-existence of streamers and blobs, which provide an experimental opportunity to validate key physics for ITER.

The possible role of electromagnetic (EM) effects in SOL simulations is now also being explored. First electromagnetic nonlinear full-f gyrokinetic simulations of turbulence on open field lines have been conducted using the GKEYLL code [119–122]. A model NSTX SOL region has been simulated using a helical, open-field-line flux-tube with field-lines intersecting metal divertor plates on either end. Changes in upstream midplane gradients and target fluxes are predicted when including EM effects for sufficiently large heating and fueling source rates, in particular a steepening of gradients crossing from source region to the source-free region (figure 15). The simulations also predict intermittent blob-like dynamics that can be statistically characterized and compared to experiment. Closed flux surfaces, shaping and X-point geometry are now being included to more realistically model the pedestal-SOL-wall dynamics.

Newly designed PFCs in the high heat flux regions of NSTX-U divertor tiles have a castellated design, in which narrow slices are cut into the graphite surface to eliminate transverse conduction. This reduces thermal stresses so that the PFC operation is instead constrained by the ~1600 °C graphite surface temperature limit associated with the onset of carbon blooms. The Heat flux Engineering Analysis Toolkit (HEAT) has been developed and applied to predict surface heat flux and temperature as a function of plasma shaping and PFC geometry by coupling magnetic equilibrium, 3D CAD, SOL physics, and finite-volume solvers [123]. Figure 16 (top) illustrates a prediction of the 3D heat flux footprint in the lower divertor of a full-field, highly-shaped NSTX-U projected scenario (1.0 T, 2.0 MA), where variations due to the castellations (and fishscaling) are apparent. Without mitigation, the prescribed PFC temperature limits can be reached within ~2.5 s at high power (10 MW). With the capability to simulate time varying discharges, additional HEAT analysis was used to predict the efficacy of strike-point sweeping on limiting PFC temperature rise. Figure 16 (bottom) shows that when the strike-point sweep frequency approaches 10 Hz, the limit is delayed until nearly 4 s and maximum temperatures are much smaller. Additional modules are being developed to incorporate SOL plasma radiation (and ELM loads) to predict PFC operational limits in additional scenarios employing radiative/detached divertors via impurity seeding.

As target heat fluxes in some high-power NSTX-U scenarios are predicted to reach values far exceeding solid material steady-state limits (as expected in reactor conditions), a number of novel liquid and evaporative lithium PFC solutions have been proposed for testing in future NSTX-U campaigns [124, 125]. Previous modelling of one such concept, the lithium vapor box [126, 127], has shown its feasibility in reducing target heat fluxes while maintaining a naturally stable detachment front due to the gradient in lithium vapor enabled by differentially pumping. Additional recent modelling has investigated the impact of additional deuterium puffing on controlling upstream lithium density [128]. SOLPS-ITER [129] simulations based on an NSTX-U experiment (with an open divertor configuration) predict that upstream lithium concentration can be kept to $n_{Li}/n_e < 2\%$ with sufficient D_2 puffing in the private flux region, while maintaining reduced target

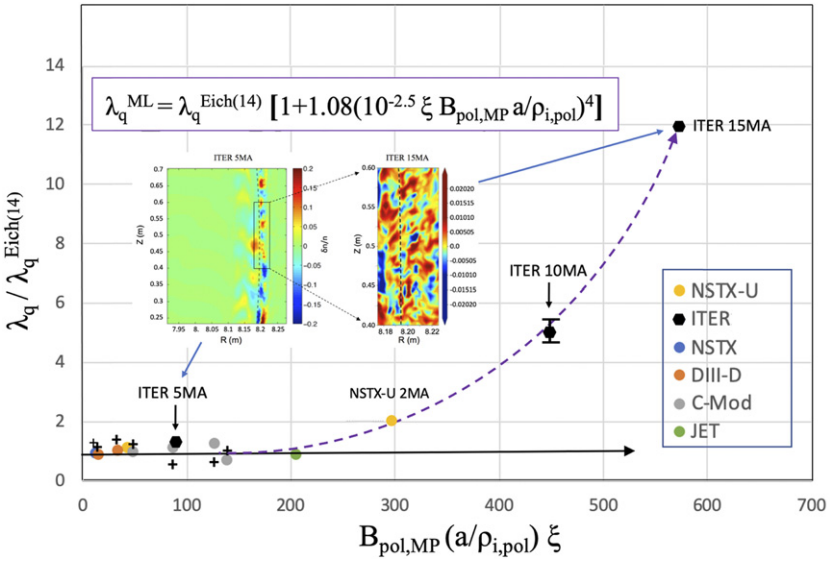

Figure 14. Predicted heat-flux width deviation (XGC1), as a ratio of the empirical scaling. Line shows new fit derived from simulations. Reproduced with permission from [118].

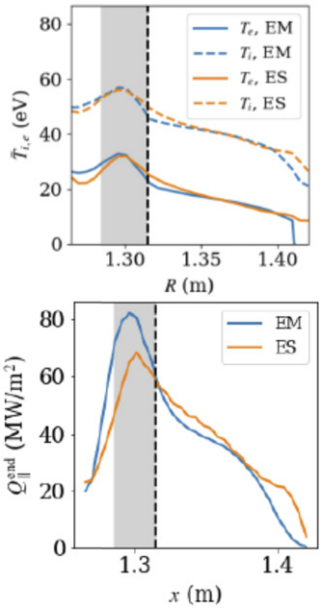

Figure 15. (Top) Upstream temperatures and (bottom) target heat fluxes predicted from electromagnetic simulations (Gkeyll) for NSTX-like model SOL. The gray regions indicate the location of particle and energy sources. Reproduced from [119].

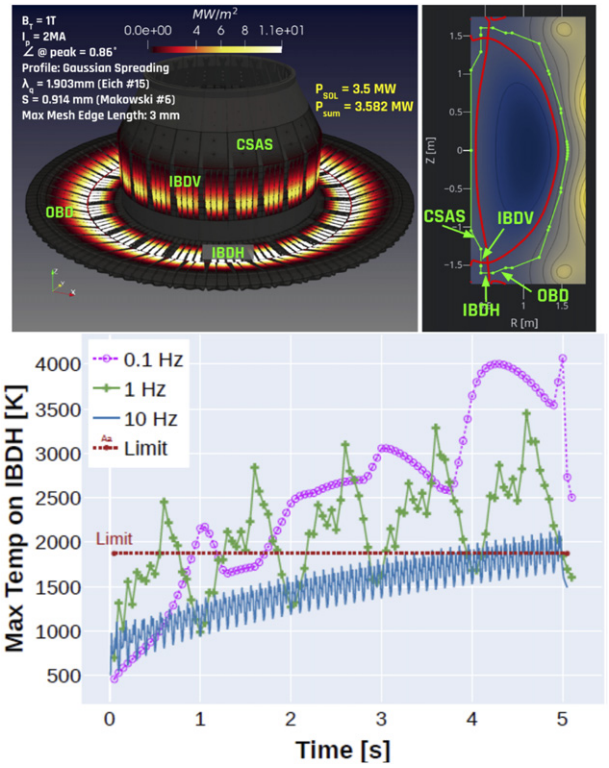

Figure 16. (Top) Predicted 3D target heat flux (HEAT) for a full-field NSTX-U projection. (Bottom) Predicted evolution of maximum PFC temperature for different strike-point sweep frequencies. [123], copyright © American Nuclear Society, reprinted by permission of Taylor & Francis Ltd, http://www.tandfonline.com on behalf of American Nuclear Society, http://www.ans.org/.

temperatures and heat fluxes in detached conditions. Future simulations will investigate the effect of divertor closure and drifts for possible future NSTX-U lithium vapor box concepts.

6. RF physics

NSTX-U is equipped with a 12-strap HHFW antenna, with up to 6 MW (30 MHz) for heating and current drive that was used on NSTX to study electron thermal transport, rotation, and EP physics [130]. In many experiments, however, a large amount of HHFW power was observed to be missing from the plasma core, correlated with the presence of bright plasma spirals in the SOL from the antenna to the divertor regions [131, 132]. Previous full-wave modelling suggested this is due to losses in the SOL from cavity modes [133, 134]. More recent modelling, using 2D full-wave simulations (FW2D) adapted to

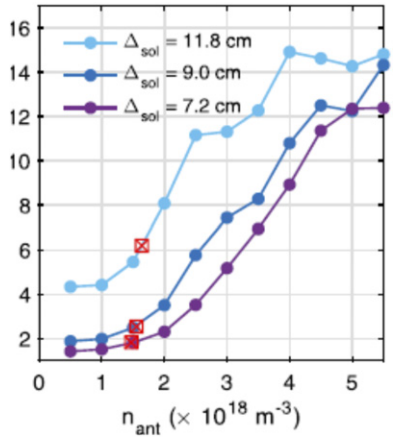

Figure 17. Predicted SOL power loss (% of HHFW injected power) vs density in front of the antenna (n_{ant}) and gap between LCFS and antenna (Δ_{SOL}). Reprinted from [135], with the permission of AIP Publishing.

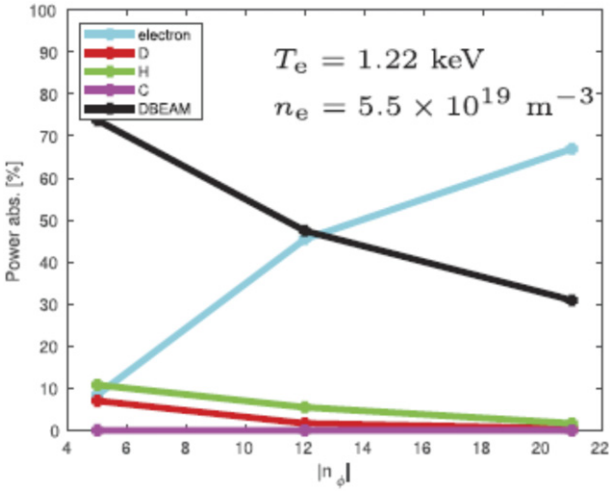

Figure 18. HHFW absorbed power vs antenna phasing, assuming 2% H in a full field NSTX-U projection. Reproduced courtesy of IAEA. Figure from [136]. Copyright (2019) IAEA.

include realistic vessel boundary shapes, has been used to further investigate the sensitivity of these losses to antenna phasing, SOL density and magnetic field strength [135]. The simulations predict that SOL losses should be reduced for larger antenna phasing and smaller density in front of the antenna (figure 17), consistent with experimental observations and previous AORSA 2D simulations. Generally it is found that losses are minimized as the density in front of the antenna approaches and drops below the fast wave cutoff density (red squares). Predicted SOL losses are further minimized for smaller distance between the LCFS and antenna, Δ_{SOL} (smaller SOL volume) and larger magnetic field, providing a route to optimization in NSTX-U.

In addition to SOL losses, the absorption of HHFW heating in the presence of NBI was observed in NSTX to be weaker than in conditions without NBI, especially to electrons. Additional 2D full-wave simulations (AORSA, using rectangular boundaries) were used to predict the competition

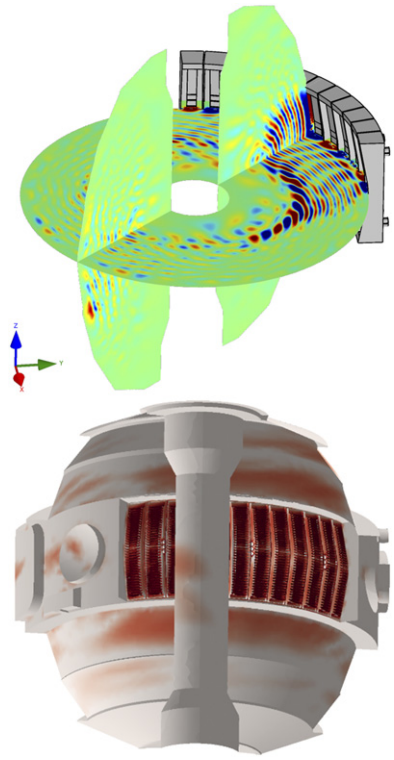

Figure 19. (Top) E_z component of the wave electric field predicted for HHFW heating (150° antenna phasing) in NSTX-U using 3D Petra-M simulations. (Bottom) Predicted electric field amplitude on the wall surface for 30° antenna phasing where stronger SOL interactions are predicted. Reproduced with permission from [140].

between electron and fast ion absorption in NSTX-U without and with NBI [136]. Assuming a Maxwellian distribution of fast ions with a temperature proportional to the effective energy computed by TRANSP/NUBEAM, the simulations predict larger absorption to electrons can be achieved when going to larger field and larger antenna phasing (∼toroidal mode number, figure 18). The electron absorption is also increased for larger ratios of T_e/T_i (with or without NBI) which can not *a priori* be predicted without more accurate transport models. The above simulations assumed a 2% hydrogen concentration based on NSTX results, which has marginal impact on absorption in simulations above (green line, figure 18). However, additional simulations at larger concentration (up to 10% H) predict more significant hydrogen absorption due to the presence of the 2nd H harmonic in the core, indicating a new possible operating regime that may be relevant to ICRH in ITER.

The various 2D simulations above provide considerable insight into how to manipulate HHFW antenna phasing, magnetic field, plasma density, and SOL geometry to minimize SOL losses and optimize thermal coupling, especially in the presence of NBI. To provide more realistic, self-consistent prediction of these effects, a state-of-the-art generic electromagnetic simulation tool for modeling RF wave propagation, Petra-M (Physics Equation Translator for MFEM [137]), has been developed [138–141]. The Petra-M framework solves Maxwell's equations in the frequency domain using realistic

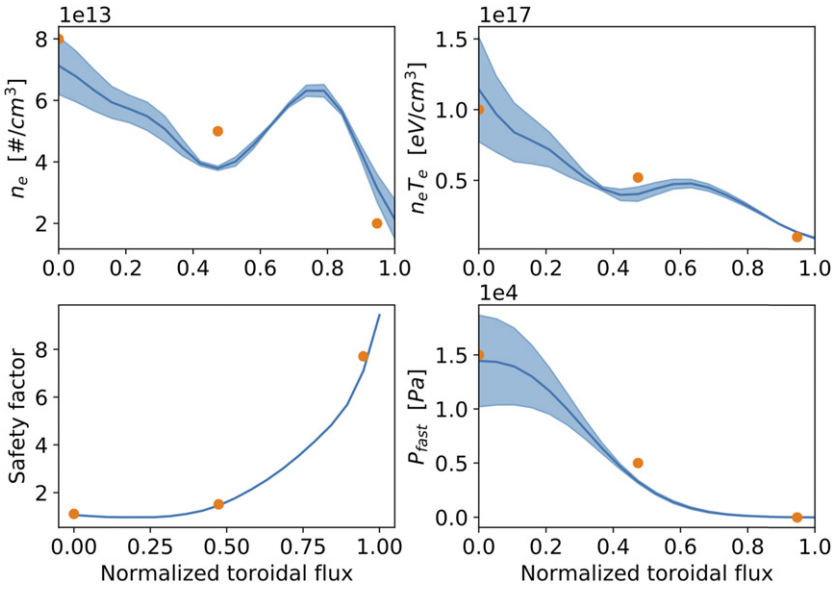

Figure 20. Optimization results comparing achieved stationary profiles as predicted by the machine-learning accelerated models (lines) with targets (orange dots). Neural network model uncertainty (standard deviation of ensemble of models) is indicated by the shaded regions. Reproduced with permission from [147].

3D CAD drawings of HHFW antenna geometry, vacuum vessel, and internal passive plates. Figure 19 (top) shows the predicted HHFW 3D electric field in a model NSTX-U scenario (using an anisotropic cold plasma model in the torus with artificial collisions), where the toroidal propagation due to high antenna phasing is apparent. Additional simulations at lower antenna phasing predict much stronger interactions in the SOL, consistent with the NSTX experimental observations. With these stronger SOL interactions at low antenna phasing, the 3D simulations also predict stronger electric fields on the internal surfaces and passive plates (figure 19, bottom) which will be important to consider for understanding RF sheath effects (planned for future implementation in Petra-M) and impurity generation.

7. Scenario optimization and control

To facilitate efficient exploration of NSTX-U operating space, multiple approaches for optimizing steady-state scenario and actuator trajectories using integrated-model-based prediction have been recently developed. Using integrated predictive TRANSP simulations, an automated iterative approach has been developed and used to optimize non-inductive ramp-up in high-performance scenario projections that identified an improved solution with respect to the original optimization performed manually [142]. While this approach is promising, convergence can take several days of calculation time. To accelerate the iterative optimization, reduced models have been proposed and implemented for current profile evolution [143] and momentum transport [144]. Machine learning neural-net approaches have also been developed to generate highly accelerated models for neutral beam heating, torque and current drive profiles based on a database of NUBEAM calculations [145]. A similar neural-net based model for predicting the normalized shape of electron density and temperature profiles was developed based on a database of experimental profiles [146]. Combined with a volume-averaged power and particle balance using confinement scalings, this model provides a fast empirically-based profile prediction capability. By combining these machine-learning accelerated approaches, optimization of stationary scenarios and actuator trajectories has been demonstrated with convergence achieved in minutes [147]. Results applying the approach are shown in figure 20, where boundary shape, plasma current, NBI power and density were optimized to best match prescribed test target profiles. The solution achieves close matching of the prescribed target points (orange markers) in electron density and pressure, safety factor profile, and fast ion pressure. The non-monotonic behaviour predicted for the electron density and pressure was observed in NSTX-U discharges as seen in figures 8 and 9 of [146]. The optimization scheme penalizes large neural network ensemble standard deviations (depicted as shaded regions) to help ensure the obtained results are from the reliably modeled operating space. Future work will focus on expanding and validating the predictive capability of the machine learning models.

While the actuator trajectories designed by the techniques described above provide guidance for achieving optimal performance, real-time feedback control algorithms and measurements are also required to reliably achieve and maintain desired stable plasma conditions. For high power NSTX-U discharges, it is expected that heat flux mitigation strategies will be needed, including control of flux expansion. To facilitate this, an algorithm for identifying and controlling the snowflake diverter configuration was developed [148]. The model-based control algorithm enables multi-input multi-output control over the diverter coils to track operator specified

snowflake diverter characteristics. In addition to shape control, a reduced-model-based feedback control of the safety factor profile was developed [149] and tested using the recently improved TRANSP closed-loop control modelling [150]. To enable fast profile measurements suitable for real-time applications, a scalable framework for Thomson scattering analysis was established using high speed analog-to-digital converters, a dedicated real-time server, and new analysis software optimized for fast and accurate fitting of the Thomson spectra [151, 152]. With these improvements, electron density and temperatures can be computed with $<$17 ms latency with accuracy that matches the slower post-shot analysis.

Modeling of both inductive and non-inductive startup methods has progressed to facilitate plasma formation in present and future tokamaks. A reduced semi-empirical model using time-dependent axisymmetric vacuum field calculations has been developed to determine optimal prefill and feed-forward coil current targets required for reliable direct induction startup on NSTX-U and MAST-U [153]. The model has recently been used to help MAST-U achieve first plasma [154]. 3D resistive MHD simulations (NIMROD [155]) of coaxial helicity injection based on NSTX experiments predict non-inductive current generation from plasmoid-mediated reconnection scales favorably to higher B_T [156]. While there are no current plans for CHI in NSTX-U, the favorable scaling implies that it may still be an effective approach for non-inductive startup in future devices operating at higher field.

8. Summary

Considerable progress has been made in validating the mechanisms responsible for core thermal transport, fast ion transport, and H-mode pedestal structure, to improve understanding of confinement scaling and achievable performance limits at low-aspect ratio. Improved modeling of global MHD and EP instabilities, as well as developments in integrated predictive modeling and real-time control methods, provide tools to help optimize scenarios in future NSTX-U experiments. Numerous observations of SOL and divertor turbulence have provided detailed measurements of dynamics that influence L/H transition, ELM onset, inter-ELM turbulence, and SOL-divertor connectivity. New simulation and modeling capabilities have been developed to predict boundary turbulence, which influences particle and heat loads to divertor targets, and to predict operational limits of PFCs. The recent results in analysis, simulation and modeling of NSTX and NSTX-U, as well as future experiments on NSTX-U and other STs [154, 157–159], continue to advance the physics basis and technical solutions required for optimizing the configuration of next-step steady-state tokamak fusion devices.

Acknowledgments

This research was supported by US DOE Contracts DE-AC02-09CH11466, DE-FG02-02ER54678, DE-FG02-99ER54518, DE-SC0013977, DE-SC0021385, DE-AC52-07NA27344, DE-SC0021271, DE-SC0021353, DE-SC0021311, DE-SC0021207, DE-SC0012890, DE-ACO5-000R22725 and the DOE Early Career Research Program. This research used resources of the National Energy Research Scientific Computing Center, a DOE Office of Science User Facility supported by US DOE Contract No. DE-AC02-05CH11231, as well as the leadership class computers Summit at OLCF and Theta at ALCF for large scale computing via INCITE award. The United States Government retains a non-exclusive, paid-up, irrevocable, world-wide license to publish or reproduce the published form of this manuscript, or allow others to do so, for United States Government purposes.

ORCID iDs

W. Guttenfelder https://orcid.org/0000-0001-8181-058X
D.J. Battaglia https://orcid.org/0000-0001-8897-9740
N. Bertelli https://orcid.org/0000-0002-9326-7585
M.D. Boyer https://orcid.org/0000-0002-6845-9155
A. Diallo https://orcid.org/0000-0002-0706-060X
V.N. Duarte https://orcid.org/0000-0001-8096-7518
E.D. Emdee https://orcid.org/0000-0003-3334-2077
N. Ferraro https://orcid.org/0000-0002-6348-7827
W. Heidbrink https://orcid.org/0000-0002-6942-8043
S.M. Kaye https://orcid.org/0000-0002-2514-1163
A. Kleiner https://orcid.org/0000-0002-5800-8027
J.B. Lestz https://orcid.org/0000-0002-6975-1537
C. Liu https://orcid.org/0000-0002-6747-955X
D. Liu https://orcid.org/0000-0001-9174-7078
R. Maingi https://orcid.org/0000-0003-1238-8121
J.R. Myra https://orcid.org/0000-0001-5939-8429
S. Munaretto https://orcid.org/0000-0003-1465-0971
M. Podestà https://orcid.org/0000-0003-4975-0585
T. Rafiq https://orcid.org/0000-0002-2164-1582
J. Ruiz Ruiz https://orcid.org/0000-0003-4258-5273
Z.R. Wang https://orcid.org/0000-0002-7496-959X
B.J.Q. Woods https://orcid.org/0000-0003-2628-3873
J. Yang https://orcid.org/0000-0001-8422-8464
S. Banerjee https://orcid.org/0000-0003-0859-8855
R.E. Bell https://orcid.org/0000-0001-9544-498X
A. Bierwage https://orcid.org/0000-0003-1243-0502
C. Clauser https://orcid.org/0000-0002-2597-5061
N. Crocker https://orcid.org/0000-0003-2379-5814
T. Evans https://orcid.org/0000-0002-8357-5859
M. Francisquez https://orcid.org/0000-0002-8247-3770
R.J. Goldston https://orcid.org/0000-0002-0368-5514
S. Jardin https://orcid.org/0000-0001-6390-6908
E. Kolemen https://orcid.org/0000-0003-4212-3247
J.D. Lore https://orcid.org/0000-0002-9192-465X
R. Lunsford https://orcid.org/0000-0003-3588-6801
J.E. Menard https://orcid.org/0000-0003-1292-3286
J.H. Nichols https://orcid.org/0000-0001-9629-2252
M. Ono https://orcid.org/0000-0001-9849-9417
J.-K. Park https://orcid.org/0000-0003-2419-8667
F. Poli https://orcid.org/0000-0003-3959-4371
D. Stotler https://orcid.org/0000-0001-5521-8718
B. Wirth https://orcid.org/0000-0002-0395-0285

References

[1] Menard J.E. *et al* 2012 *Nucl. Fusion* **52** 083015
[2] Gerhardt S.P., Andre R. and Menard J.E. 2012 *Nucl. Fusion* **52** 083020
[3] Menard J.E. *et al* 2011 *Nucl. Fusion* **51** 103014
[4] Menard J.E. *et al* 2016 *Nucl. Fusion* **56** 106023
[5] Menard J. E. *et al* 2019 *Phil. Trans. R. Soc.* A **377** 20170440
[6] Menard J.E. *et al* 2022 *Nucl. Fusion* **62** 036026
[7] Sykes A. *et al* 1997 *Plasma Phys. Control. Fusion* **39** B247
[8] Sabbagh S. *et al* 2013 *Nucl. Fusion* **53** 104007
[9] Harrison J.R. *et al* 2019 *Nucl. Fusion* **59** 112011
[10] Gusev V.K. *et al* 2009 *Nucl. Fusion* **49** 104021
[11] Valovic M. *et al* 2011 *Nucl. Fusion* **51** 073045
[12] Kaye S.M., Gerhardt S., Guttenfelder W., Maingi R., Bell R.E., Diallo A., LeBlanc B.P. and Podesta M. 2013 *Nucl. Fusion* **53** 063005
[13] Buxton P.F., Connor J.W., Costley A.E., Gryaznevich M.P. and McNamara S. 2019 *Plasma Phys. Control. Fusion* **61** 035006
[14] Kurskiev G.S. *et al* 2019 *Nucl. Fusion* **59** 066032
[15] Kurskiev G.S. *et al* 2021 *Nucl. Fusion* **61** 064001
[16] Gerhardt S.P. *et al* 2021 IAEA-FEC TECH/P3-17
[17] Menard J.E. *et al* 2017 *Nucl. Fusion* **57** 102006
[18] Battaglia D.J. *et al* 2018 *Nucl. Fusion* **58** 046010
[19] Kaye S.M. *et al* 2019 *Nucl. Fusion* **59** 112007
[20] Gerhardt S.P. *et al* 2011 *Nucl. Fusion* **51** 073031
[21] Wang Z., Glasser A.H., Brennan D., Liu Y. and Park J. 2020 *Phys. Plasmas* **27** 122503
[22] Glasser A.H., Wang Z.R. and Park J.-K. 2016 *Phys. Plasmas* **23** 112506
[23] Kim S.H., Bulmer R.H., Campbell D.J., Casper T.A., LoDestro L.L., Meyer W.H., Pearlstein L.D. and Snipes J.A. 2016 *Nucl. Fusion* **56** 126002
[24] Park J.-K., Boozer A.H. and Glasser A.H. 2007 *Phys. Plasmas* **14** 052110
[25] Ferraro N.M. 2012 *Phys. Plasmas* **19** 056105
[26] Ferraro N.M., Park J.-K., Myers C.E., Brooks A., Gerhardt S.P., Menard J.E., Munaretto S. and Reinke M.L. 2019 *Nucl. Fusion* **59** 086021
[27] Munaretto S., Evans T.E., Ferraro N.M., Orlov D.M., Trevisan G.L. and Wu W. 2019 *Nucl. Fusion* **59** 076039
[28] Lyons B.C., Kim C.C., Liu Y.Q., Ferraro N.M., Jardin S.C., McClenaghan J., Parks P.B. and Lao L.L. 2019 *Plasma Phys. Control. Fusion* **61** 064001
[29] Ferraro N.M., Lyons B.C., Kim C.C., Liu Y.Q. and Jardin S.C. 2019 *Nucl. Fusion* **59** 016001
[30] Ferraro N.M., Jardin S.C., Lao L.L., Shephard M.S. and Zhang F. 2016 *Phys. Plasmas* **23** 056114
[31] Raman R., Lay W.-S., Jarboe T.R., Menard J.E. and Ono M. 2019 *Nucl. Fusion* **59** 016021
[32] Raman R. *et al* 2021 *Nucl. Fusion* **61** 126034 Submitted
[33] Clauser C.F. *et al* 2021 *Nucl. Fusion* **61** 116003
[34] Bardóczi M. *et al* 2019 *Nucl. Fusion* **59** 106013
[35] Podesta M. *et al* 2021 IAEA FEC TH/P1-26
[36] Yang J., Podestà M. and Fredrickson E.D. 2021 *Plasma Phys. Control. Fusion* **63** 045003
[37] White R.B. and Chance M.S. 1984 *Phys. Fluids* **27** 2455
[38] Breslau J. *et al* 2018 TRANSP [Computer Software]
[39] Pankin A., McCune D., Andre R., Bateman G. and Kritz A. 2004 *Comput. Phys. Commun.* **159** 157
[40] Liu C. *et al* 2022 *Comput. Phys. Commun.* **275** 108313
[41] Duarte V.N. *et al* 2017 *Nucl. Fusion* **57** 054001
[42] Duarte V.N., Berk H.L., Gorelenkov N.N., Heidbrink W.W., Kramer G.J., Nazikian R., Pace D.C., Podestà M. and Van Zeeland M.A. 2017 *Phys. Plasmas* **24** 122508
[43] Duarte V.N., Gorelenkov N.N., Schneller M., Fredrickson E.D., Podestà M. and Berk H.L. 2018 *Nucl. Fusion* **58** 082013
[44] Woods B.J.Q. *et al* 2020 *IEEE Trans. Plasma Sci.* **48** 71
[45] Fredrickson E.D., Gorelenkov N.N., Podesta M., Bortolon A., Gerhardt S.P., Bell R.E., Diallo A. and LeBlanc B. 2014 *Nucl. Fusion* **54** 093007
[46] White R.B., Duarte V.N., Gorelenkov N.N., Fredrickson E.D., Podestà M. and Berk H.L. 2019 *Phys. Plasmas* **26** 092103
[47] Berk H.L., Breizman B.N. and Petviashvili N.V. 1997 *Phys. Lett.* A **234** 213
[48] White R.B., Duarte V.N., Gorelenkov N.N., Fredrickson E.D. and Podesta M. 2020 *Phys. Plasmas* **27** 052108
[49] White R.B. *et al* 2021 IAEA FEC TH/P1-13
[50] Bierwage A., White R.B. and Duarte V.N. 2021 *Plasma Fusion Res.* **16** 1403087
[51] White R.B., Duarte V.N., Gorelenkov N.N., Fredrickson E.D. and Podesta M. 2020 *Phys. Plasmas* **27** 022117
[52] Stutman D. *et al* 2009 *Phys. Rev. Lett.* **102** 115002
[53] Gorelenkov N.N., Stutman D., Tritz K., Boozer A., Delgado-Aparicio L., Fredrickson E., Kaye S. and White R. 2010 *Nucl. Fusion* **50** 084012
[54] Kolesnichenko Y.I. *et al* 2010 *Phys. Rev. Lett.* **104** 075001
[55] Belova E.V. *et al* 2015 *Phys. Rev. Lett.* **115** 015001
[56] Lestz J.B., Belova E.V. and Gorelenkov N.N. 2021 *Nucl. Fusion* **61** 086016
[57] Lestz J.B., Gorelenkov N.N., Belova E.V., Tang S.X. and Crocker N.A. 2020 *Phys. Plasmas* **27** 022513
[58] Lestz J.B., Gorelenkov N.N., Belova E.V., Tang S.X. and Crocker N.A. 2020 *Phys. Plasmas* **27** 022512
[59] Fredrickson E. *et al* 2017 *Phys. Rev. Lett.* **118** 265001
[60] Fredrickson E.D. *et al* 2018 *Nucl. Fusion* **58** 082022
[61] Belova E. *et al* 2019 *Phys. Plasmas* **26** 092507
[62] Belova E. *et al* 2021 IAEA FEC TH/P1-27
[63] Fredrickson E. *et al* 2019 *Phys. Plasmas* **26** 032111
[64] Fredrickson E. *et al* 2021 IAEA FEC EX/P7-6 (accepted)
[65] Ren Y. *et al* 2017 *Nucl. Fusion* **57** 072002
[66] Ren Y. *et al* 2019 *Nucl. Fusion* **59** 096045
[67] Guttenfelder W. *et al* 2013 *Nucl. Fusion* **53** 093022
[68] Ruiz Ruiz J. *et al* 2020 *Plasma Phys. Control. Fusion* **62** 075001
[69] Candy J. and Waltz R.E. 2003 *J. Comput. Phys.* **186** 545
[70] Ruiz Ruiz J. *et al* 2015 *Phys. Plasmas* **22** 122501
[71] Ruiz Ruiz J. *et al* 2019 *Plasma Phys. Control. Fusion* **61** 115015
[72] Ruiz Ruiz J. *et al* 2020 *Phys. Plasmas* **27** 122505
[73] Howard N.T. *et al* 2016 *Phys. Plasmas* **23** 056109
[74] Holland C.H. *et al* 2017 *Nucl. Fusion* **57** 066043
[75] Staebler G.M. *et al* 2017 *Nucl. Fusion* **57** 066046
[76] Ren Y. *et al* 2020 *Nucl. Fusion* **60** 026005
[77] Chen X. *et al* 2021 *Rev. Sci. Instrum.* **92** 053537
[78] Guttenfelder W. *et al* 2019 *Nucl. Fusion* **59** 056027
[79] Guttenfelder W. *et al* 2011 *Phys. Rev. Lett.* **106** 155004
[80] Guttenfelder W. *et al* 2012 *Phys. Plasmas* **19** 022506
[81] Guttenfelder W. *et al* 2012 *Phys. Plasmas* **19** 056119
[82] Kaye S.M. 2014 *Phys. Plasmas* **21** 082510
[83] Rafiq T. *et al* 2016 *Phys. Plasmas* **23** 062507
[84] Rafiq T. *et al* 2021 *Phys. Plasmas* **28** 022504
[85] Rechester A.B. and Rosenbluth M.N. 1978 *Phys. Rev. Lett.* **40** 38
[86] Rafiq T. *et al* 2013 *Phys. Plasmas* **20** 032506
[87] Scotti F. *et al* 2013 *Nucl. Fusion* **53** 083001
[88] Howard N. *et al* 2020 IAEA FEC PD/1-1
[89] Belli E.A. and Candy J. 2008 *Plasma Phys. Control. Fusion* **50** 095010
[90] Belli E.A. and Candy J. 2012 *Plasma Phys. Control. Fusion* **54** 015015

[91] Candy J., Belli E.A. and Bravenec R.V. 2016 *J. Comput. Phys.* **324** 73
[92] Maingi R. *et al* 2009 *Phys. Rev. Lett.* **103** 075001
[93] Gerhardt S.P. *et al* 2014 *Nucl. Fusion* **54** 083021
[94] Battaglia D.J. *et al* 2020 *Phys. Plasmas* **27** 072511
[95] Snyder P.B. *et al* 2009 *Phys. Plasmas* **16** 056118
[96] Snyder P.B. *et al* 2011 *Nucl. Fusion* **51** 103016
[97] Boyle D.P. *et al* 2011 *Plasma Phys. Control. Fusion* **53** 105011
[98] Sontag A. *et al* 2011 *Nucl. Fusion* **51** 103022
[99] Diallo A. *et al* 2011 *Nucl. Fusion* **51** 103031
[100] Diallo A. *et al* 2013 *Nucl. Fusion* **53** 093026
[101] Kleiner A. *et al* 2021 *Nucl. Fusion* **61** 064002
[102] Scotti F. *et al* 2021 *Nucl. Fusion* **61** 036002
[103] Stotler D. and Karney C. 1994 *Contrib. Plasma Phys.* **34** 392
[104] Zweben S. *et al* 2015 *Nucl. Fusion* **55** 093035
[105] Zweben S. *et al* 2021 *Phys. Plasmas* **28** 032304
[106] Zweben S. *et al* 2019 *Phys. Plasmas* **26** 072502
[107] Zweben S. *et al* 2020 *Phys. Plasmas* **27** 052505
[108] Lampert M. *et al* 2021 *Phys. Plasmas* **28** 022304
[109] Myra J. 2007 *Phys. Plasmas* **14** 102314
[110] Ebrahimi F. 2017 *Phys. Plasmas* **24** 056119
[111] Scotti F. *et al* 2020 *Nucl. Fusion* **60** 026004
[112] Myra J. *et al* 2006 *Phys. Plasmas* **13** 112502
[113] Ku S.-H. *et al* 2018 *Phys. Plasmas* **25** 056107
[114] Eich T. *et al* 2011 *Phys. Rev. Lett.* **107** 215001
[115] Eich T. *et al* 2013 *Nucl. Fusion* **53** 093031
[116] Chang C.S. *et al* 2017 *Nucl. Fusion* **57** 116023
[117] Chang C.S. *et al* 2021 *Phys. Plasmas* **28** 022501
[118] Chang C.S. *et al* 2021 IAEA FEC TH/P4-4
[119] Mandell N. *et al* 2020 *J. Plasma Phys.* **86** 905860109
[120] Mandell N. 2021 *PhD Thesis* Princeton University
[121] Hakim A.H. *et al* 2020 *Phys. Plasmas* **27** 042304
[122] Hakim A.H. *et al* 2021 IAEA FEC TH/3-4
[123] Looby T. *et al* 2022 *Fus. Sci. Tech.* **78** 10
[124] Ono M. and Raman R. 2020 *J. Fusion Energy* **39** 402
[125] Ono M. *et al* 2021 IAEA FEC TECH/P7-11
[126] Goldston R.J. *et al* 2016 *Phys. Scr.* **T167** 014017
[127] Emdee E. *et al* 2019 *Nucl. Mat. Energy* **19** 244
[128] Emdee E. *et al* 2021 *Nucl. Mat. Energy* **27** 101004
[129] Wiesen S. *et al* 2015 *J. Nucl. Mater.* **463** 480
[130] Taylor G. *et al* 2010 *Phys. Plasmas* **17** 056114
[131] Hosea J.C. *et al* 2008 *Phys. Plasmas* **15** 056104
[132] Perkins R.J. *et al* 2012 *Phys. Rev. Lett.* **109** 045001
[133] Bertelli N. *et al* 2014 *Nucl. Fusion* **54** 083004
[134] Bertelli N. *et al* 2016 *Nucl. Fusion* **56** 016019
[135] Kim E.-H. *et al* 2019 *Phys. Plasmas* **26** 062501
[136] Bertelli N. *et al* 2019 *Nucl. Fusion* **59** 086006
[137] (https://mfem.org)
[138] Shiraiwa S. *et al* 2017 *EPJ Web Conf.* **157** 03048
[139] Bertelli N. *et al* 2020 *AIP Conf. Proc.* **2254** 030001
[140] Shiraiwa S. *et al* 2021 IAEA FEC TH/7-2
[141] Bertelli N. *et al* 2021 IAEA FEC TH/P2-16
[142] Wehner W.P. *et al* 2019 *Fusion Eng. Design* **146** 547
[143] Ilhan Z.O. *et al* 2017 *Fusion Eng. Design* **123** 564
[144] Goumiri I.R. *et al* 2017 *Phys. Plasmas* **24** 056101
[145] Boyer M.D. *et al* 2019 *Nucl. Fusion* **59** 056008
[146] Boyer M.D. *et al* 2021 *Nucl. Fusion* **61** 046024
[147] Boyer M.D. *et al* 2021 IAEA FEC EX/P7-5
[148] Vail P.J. *et al* 2019 *Plasma Phys. Control. Fusion* **61** 035005
[149] Ilhan Z.O. *et al* 2019 *Fusion Eng. Design* **146** 555
[150] Boyer M.D. *et al* 2020 *Nucl. Fusion* **60** 096007
[151] Laggner F. *et al* 2019 *Rev. Sci. Instrum.* **90** 043501
[152] Rozenblat R. *et al* 2019 *Fus. Sci. Technol.* **75** 835
[153] Battaglia D.J. *et al* 2019 *Nucl. Fusion* **59** 126016
[154] Harrison J. *et al* 2021 IAEA FEC EX/P6-39
[155] Sovinec C.R. *et al* 2004 *J. Comp. Phys.* **195** 355
[156] Ebrahimi F. 2019 *Phys. Plasmas* **26** 092502
[157] Takase Y. *et al* 2022 *Nucl. Fusion* **62** 042011
[158] Petrov Y.V. *et al* 2022 *Nucl. Fusion* **62** 042009
[159] Gryaznevich M. *et al* 2021 IAEA FEC OV/4-5Rd (accepted)